Electrochemical analysis of BaZr<sub>0.8</sub>Y<sub>0.2</sub>O<sub>3-δ</sub>-Gd<sub>0.2</sub>Ce<sub>0.8</sub>O<sub>2-δ</sub> composite

electrolytes by distribution of relaxation time method

Pan Xu<sup>a</sup>, Yihang Li<sup>a</sup>, Tong Liu<sup>b</sup>, Fanglin Chen<sup>c</sup>, Weiwei Wu a<sup>\*</sup>, Cong Ren<sup>a\*</sup>

<sup>a</sup> Department of Applied Chemistry, School of Advanced Materials and Nanotechnology,

Xidian University, Xi'an 710071, P. R. China.

<sup>b</sup> Key Laboratory of Hydraulic Machinery Transients (Wuhan University), Ministry of

Education, School of Power and Mechanical Engineering, Wuhan University, Wuhan,

Hubei 430072, China

<sup>c</sup> Department of Mechanical Engineering, University of South Carolina, Columbia, SC

29208, USA

\*Corresponding authors:

E-mail: wwwu@xidian.edu.cn (W.W.Wu) & cren@xidian.edu.cn (C. Ren)

Highlight

Composite electrolyte is fabricated by combining proton and oxygen-ion conductor.

Sinterability of the electrolyte is improved by introducing GDC into BZY.

Impedance data is analyzed by DRT method, revealing the hetero-phase grain

boundary at lower temperature.

Conductivity of composite electrolyte is enhanced in both oxidizing and reducing

atmospheres.

Abstract

 $BaZr_{0.8}Y_{0.2}O_{3-\delta}$  (BZY)- $Gd_{0.20}Ce_{0.80}O_{2-\delta}$  (GDC) composite electrolytes have been

fabricated by mechanical mixing the BZY and GDC powders with different weight ratio

(30 wt%, 50 wt % and 70 wt %). The ceramic powders were synthesized by a sol-gel

method, and the crystalline structure of the ceramic powders and composite electrolytes

was examined by X-ray diffraction (XRD). Good chemical compatibility between BZY

and GDC has been shown based on the XRD analysis. The morphology and element

distribution of the BZY and composite electrolyte were observed by the scanning

1

electron microscope (SEM) and energy dispersive x-ray spectroscopy (EDX). The conductivity measurement was conducted in both oxidizing and reducing atmospheres by the means of electrochemical impedance spectroscopy (EIS). The equivalent circuit and distribution of relaxation times (DRT) method were employed to analyze the obtained EIS data. For the composite electrolytes, two different types of grain boundaries can be identified in the DRT diagram derived from the impedance data measured in reducing atmosphere at lower temperature (< 450 °C). The influence of the GDC content on the resistance between the two grain boundaries was investigated and the result can be attributed to the different average grain size of the samples. The total conductivity of the composite electrolytes in each atmosphere was also analyzed and discussed, and the composition of 30wt%BZY-70%GDC (BG37) shows the highest conductivity of 0.0269 Scm<sup>-1</sup> at 700 °C in reducing atmosphere. Single cell based on BG37 electrolyte was fabricated and tested, maximum power density of 0.442 Wcm<sup>-2</sup> at 700 °C with the OCV of 0.89V were achieved.

Key words: B: Grain boundaries; C: Impedance; C: Ionic conductivity; E: Fuel cells.

#### 1. Introduction

Solid oxide fuel cells (SOFCs) have been regarded as a promising next-generation energy conversion technology due to their advantages such as high energy conversion efficiency, fuel flexibility, and low pollution[1-3]. The traditional SOFCs based on fluorite-structured yttrium-stabilized zirconia (YSZ) electrolyte usually operate at high temperature (from 800 °C to 1000 °C) to ensure a good cell performance. However, high operation temperature usually results in many problems such as narrowing the choice of the sealing materials, potential reaction between cell components, thermal expansion mismatch and slow start-up. Therefore, lowering the SOFC operation temperature while maintaining favorable cell performance is needed for the successful commercialization of SOFCs. To operate the SOFCs at lower temperature (below 700 °C) with good performance, the ohmic resistance of the cell, which is dominated from the electrolyte, should be decreased. One widely adopted approach is to fabricate

thin-film electrolyte [4], and the other is to explore novel electrolyte materials with higher ionic conductivity at reduced temperatures [5]. Various materials have been explored as the electrolyte for SOFCs operating at reduced temperatures; ceria-based oxide ion-conductor and barium-based proton-conductor are two main material systems that have been extensively investigated. The doped ceria (Ce<sub>0.8</sub>Gd<sub>0.2</sub>O<sub>1.9</sub>, GDC or Ce<sub>0.8</sub>Sm<sub>0.2</sub>O<sub>1.9</sub>, SDC) shows much higher oxide ionic conductivity than the traditional yttria-stabilized zirconia (YSZ) at lower temperatures [6-8], but under reducing atmosphere or low oxygen partial pressures, cerium ion will change its valance state from Ce<sup>+4</sup> to Ce<sup>+3</sup> through Eq.1 [9]. The reduction of cerium ions induces electronic conduction in the electrolyte, which leads to a voltage loss of the SOFCs and causes a deterioration of mechanical strength of the ceria-based electrolyte.

$$4CeO_2 \longrightarrow 2Ce_2O_3 + O_2 \tag{1}$$

Barium-based oxides, typically yttrium doped BaCeO<sub>3</sub> (BCY) and yttrium doped BaZrO<sub>3</sub> (BaZr<sub>0.8</sub>Y<sub>0.2</sub>O<sub>3-δ</sub>, BZY), showing protonic conductivity at reduced temperatures in humid air or hydrogen atmosphere, have been extensively studied as the electrolyte for proton conducting solid oxide fuel cell (PC-SOFC) [10, 11]. BCY demonstrates higher conductivity and better sintering property than BZY, however, it easily reacts with CO<sub>2</sub>, water vapor and H<sub>2</sub>S. Consequently, cells based on BCY electrolyte usually exhibit considerable performance degradation [12-14]. BZY shows better chemical stability than BCY, however, it has drawbacks such as poor sinterability and low grain boundary conductivity. To enhance the sinterability and grain growth of BZY, various metal oxides or non-metal oxides are employed as the sintering-aids. NiO, CuO, ZnO and P<sub>2</sub>O<sub>5</sub> can effectively reduce the sintering temperature of BZY to around 1400 °C and most of them have already been used for SOFC fabrication[15-19]. However, BZY samples sintered with sintering aids often show a lower total conductivity than the sintered BZY samples without sintering aids. It has been an important issue to enhance the sinterability of the BZY electrolyte while maintaining an adequate ionic conductivity.

To improve the electrolyte properties at lower operation temperature, another

effective strategy is to fabricate the composite electrolyte[20, 21], especially the proton/oxide ion conducting composite electrolyte. Luo et. al fabricated the BZY-YSZ composite ceramics (BZY with 50wt% YSZ) and reported an enhancement of sinterability comparing with BZY sintered at 1450 °C for 6 hours [22]. Composite ceramics consisting of ceria-based oxide ion conductor and barium-based proton conductor have also been studied [23], revealing that barium-based ceramic can block the electronic leakage of the ceria-based electrolyte while the total conductivity could be improved due to the extra electronic conduction of ceria-based ceramics introduced under hydrogen atmosphere. Recently, Yu et. al. also reported a novel LSGM-BZCY composite electrolyte with an enhanced conductivity as well as sinterability, and ascribed these improvements to the introduction of the LSGM phase[24].

Although many composite electrolyte materials have been designed and applied for SOFC fabrication, detailed investigation on the electrical properties of the two-phase ceramic system is still limited. Especially, the reported two types of grain boundary existed in the composite electrolyte are seldom discussed[25]. In this study, BZY-GDC composite electrolytes were fabricated, their crystalline structure, sinterability and composition were characterized. The electrical conductivities of the composite electrolytes were investigated by AC impedance measurements under different atmospheres and the EIS results were further analyzed by the DRT method combing with the equivalent circuit model fitting.

## 2. Experimental

### 2.1 Powders synthesis, symmetric cells and single cell fabrication

The ceramic powder was synthesized by a sol-gel method[26]. Ba(NO<sub>3</sub>)<sub>2</sub> (Sinopharm Chemical Reagent Co. Ltd., 99%), Zr(NO<sub>3</sub>)<sub>4</sub>·5H<sub>2</sub>O (Macklin, 99.99%), Y(NO<sub>3</sub>)<sub>3</sub>·6H<sub>2</sub>O (Macklin, 99.5%) were weighed with the stoichiometric ratio of BaZr<sub>0.8</sub>Y<sub>0.2</sub>O<sub>3-δ</sub> and then dissolved in deionized water with a total metal ion concentration of 0.1M. Subsequently, acrylamide (AM, Aladdin, 99%) and N,N-methylenebisacrylamide (MBAM, Aladdin, 97%) were added to prepare a transparent stable solution. α-azoisobutyronitrile (AIBN, Aladdin, 98%) was then added to the solution as the crosslinking agent to initiate the gelation process at 80 °C and gel containing well distributed

metal ions was finally obtained. The prepared gel was dried at 90 °C for 12h to dehydrate, and then ball milled 30 mins with zirconia milling media. The milled powder was calcined at 800°C for 2 hours with a heating rate of 2 °C/min to remove the organic residue and the obtained ceramic powder was ready for electrolyte fabrication. The GDC powder was also prepared by the same method as described above. Ce(NO<sub>3</sub>)<sub>3</sub>·6H<sub>2</sub>O (Sinopharm Chemical Reagent Co., Ltd.,99%) and Gd(NO<sub>3</sub>)<sub>2</sub>·6H<sub>2</sub>O (Aladdin, 99.99%) were used as the starting materials. BZY-GDC composite materials were prepared by mixing the BZY powder with different amount of GDC powder in different weight ratio of 30, 50 and 70 wt%, denoted as BG73, BG55 and BG37, respectively, and the composite powders were then ball milled in ethanol for 10 hours. Electrolyte pellets in diameter of 13mm were fabricated by uniaxially pressing the ceramic powder under 20 MPa for 5 min and then sintered at 1550°C for 24 hours to ensure adequate density for conductivity measurement. The symmetric cells were fabricated with the cell configuration of Pt|BZY|Pt, Pt|GDC|Pt and Pt|BZY-GDC|Pt. All the surfaces of electrolyte pellets were polished and ultrasonically cleaned in ethanol to remove any impurities that may form during the sintering process. Platinum slurry with an area of 0.28 cm<sup>2</sup> was brushed on both sides of the electrolyte and sintered at 1000°C for 3 hours with a heating rate of 2 °C/min to serve as the electrodes.

The single cell with the BG37 electrolyte, GDC-NiO anode and GDC-SmBaCo<sub>2</sub>O<sub>5+δ</sub> (SBCO) cathode was fabricated by the co-pressing technique. The SBCO powder was also synthesized by the mentioned sol-gel method, anode support with electrolyte was co-pressed and sintered at 1550 °C for 6 hours to ensure a dense electrolyte. Cathode powder was prepared by mixing the GDC and SBCO powders with a weight ratio of 3:7 and then milled with terpineol to form the cathode slurry. The cathode was brush painted on the electrolyte with an area of 0.28 cm<sup>2</sup> and calcined at 1050 °C for 3 hours with a heating rate of 2 °C/min.

### 2.2 Characterization

The phase compositions of the ceramic powders and electrolytes were analyzed by powder X-ray diffraction (XRD) using a Bruker D8 Advance X-ray diffractometer. The microstructure of all electrolyte samples was observed by scanning electron

microscope (SEM) (Thermo-Fisher Scientific FEI Apero) and the elemental composition of BZY-GDC electrolyte was examined using the energy dispersive x-ray spectroscopy (EDX) system attached to the SEM. The average grain size of samples was estimated from the SEM images using Nano Measurer 1.2. The densities of the sintered electrolyte pellets were measured through the Archimedes water displacement method. The electrochemical impedance spectra of all symmetric cells were measured with an A.C. amplitude of 30 mV in the frequency ranging from 0.1 Hz to 1 MHz using a Solartron XM electrochemical workstation. The EIS measurement was conducted in dry air (ambient atmosphere) and wet hydrogen atmosphere (10 vol% H<sub>2</sub> with Ar as balance and 3 vol% H<sub>2</sub>O by flowing through a water bubbler) with a flow rate of 40 SCCM from 350 to 700°C with an interval of 50 °C. The obtained EIS data of composite electrolytes were further analyzed by the distribution of relaxation time (DRT) method and fitted with equivalent circuit model built according to the DRT result. Moreover, the conductivity of GDC electrolyte was also measured in both air and reducing atmosphere with the same test conductions of the composite electrolytes. The single cell was tested from 600 °C to 700 °C using humidified H<sub>2</sub> (3 vol% H<sub>2</sub>O) as fuel with the flow rate of 40 SCCM for the anode and ambient air as the oxidant for the cathode. The EIS and i-V curve were also measured by the Solartron XM electrochemical workstation and the EIS of single cell was performed with the same condition mentioned above.

## 3. Results and discussion

### 3.1 Crystal structural analysis

Fig.1 is the XRD pattern of the synthesized BZY (Fig.1(a)), GDC (Fig.1(b)) and SBCO cathode powders ((Fig.1(c)) calcined at different temperature. For the BZY powder, it starts to crystalize to the single-phase perovskite structure after calcined above 800 °C and there are no secondary phases observed after sintered at 1200 °C. The GDC powder can form a cubic fluorite phase without impurities after calcined at 700 °C for 2 hours. The result suggests that the acrylamide gelification process is an effectively method for ceramic powder synthesis at lower temperature. For the SBCO cathode, a typical double-perovskite structure could be obtained after sintered at 1000 °C for 2

hours. Fig.2 shows the XRD pattern of BZY-GDC composite electrolyte BG73, BG55 and BG37 after sintered at the temperature for electrolyte fabrication (1550 °C). For all the composite ceramic samples, there are no secondary phases or intermediate phases observed, indicating that BZY and GDC have good chemical compatibility even after high temperature sintering (1550 °C).

## 3.2 Morphology and sintering property

Fig.3 and Fig.4 show the surface and fracture SEM images of different samples sintered at 1550°C for 24 hours. Based on the SEM images, all the samples exhibit dense morphology without apparent pores, and the relative density of sample BZY, BG73, BG55 and BG37 were determined by the Archimedes method and the corresponding value was 93.5%, 96.6%, 96.2% and 95.2%, respectively. It can be concluded that the present of GDC content can enhance the sinterability of the samples. The average grain size of the samples was also estimated based on the surface SEM images, and the samples BZY, BG73, BG55 and BG 37 exhibit a grain size of 1.25μm, 0.94μm, 1.09μm and 2.18μm, respectively. Samples BG73 and BG55 show smaller average grain size and the same tendency has also been reported by Wang et.al. [25]. The result has been ascribed to the different grain growth rates of two materials[23].

The different phases of the BZY-GDC composite electrolyte cannot be effectively identified by analyzing the backscattered electron (BSE) image due to the relatively similar values of Ce<sup>3+</sup>, Ba<sup>2+</sup> and Zr<sup>3+</sup> [27]. Therefore, the EDX element mapping was employed to distinguish the two different grains. Fig. 5 is the EDX area map of sample BG37 and its corresponding SEM image. By comparing the SEM image and element mapping result of BG37 in the same area, the BZY and GDC grains can be identified and labeled in Fig. 5 (f), showing that GDC has larger grain size than BZY, and this result is also ascribed to the different grain growth rate of BZY and GDC [23].

## 3.3 Impedance analysis of composite electrolyte

The conductivity of the composite electrolyte was measured by EIS under dry air and humidified H<sub>2</sub> conditions. Fig.6 (a) shows the Nyquist plots of the GDC-BZY composite electrolyte in reducing atmosphere at 350 °C. The impedance spectrum typically consists of three semi-circles at lower temperature, corresponding to the bulk

resistance (R<sub>bulk</sub>), grain boundary resistance (R<sub>gb</sub>) and electrode resistance (R<sub>el</sub>) from high to low frequencies. The first arc starts to disappear with the increase of temperature due to the different relaxation time constant of the different processes involved in the symmetrical cell test[28], and the R<sub>bulk</sub> can be obtained from the intersection with the X-axis at high frequencies. In this work, the EIS of BG37 start to intersect with the Xaxis when the test temperature is higher than 450°C, as shown in Fig.7. These results suggest that the total resistance of the symmetrical cells is significantly affected by the GDC content in the electrolyte. The obtained impedance data are fitted by two types of equivalent circuit models, one for lower temperature results (\$\leq 450^{\circ}C\right) showing in Fig. 6 (b), the other one for the data tested at higher temperature, containing only two parallel R-CPE elements representing the grain boundary transport and electrode process respectively, as shown in Fig.6 (c). Through the data fitting, the bulk, grain boundary and electrode process can be separated. However, for the two-phase composite electrolyte, it has been reported that there exist two types of grain boundary processes [25]. Consequently, the conventional equivalent circuit models mentioned above are not consistent with the real electrochemical process of the symmetrical cell.

To better distinguish the bulk and grain boundary resistances, the distribution of relaxation times (DRT) technique has been applied to interpret the EIS data. According to this method, the total impedance and the distribution function of relaxation times have the following relation:

$$Z(\omega) = R_0 + R_{pol} \int_0^\infty \frac{\gamma(\tau)}{1 + j\omega\tau} d\tau$$
 (2)

where  $Z(\omega)$  is the total impedance resistance,  $R_0$  and  $R_{pol}$  are the ohmic and polarization resistance respectively,  $\gamma(\tau)$  is the distribution function of relaxation times,  $\tau$  is the relaxation time,  $\omega$  is the angular frequency and j is the imaginary unit[29]. To solve the  $\gamma(\tau)$ , which corresponds to the different relaxation time ( $\tau$ ), the DRT diagram can be obtained. For the EIS of all samples tested at 350 °C in reducing atmosphere, the DRT analysis has been conducted using the DRTTOOLS developed by Ciucci et al. based on the Tikhonov regularization with continuous function discretization [30]. The regularization method and the regularization parameter chosen for the DRT analysis are

Gaussian and  $10^{-4}$ , respectively. Then, to better analyze the EIS data measured, equivalent circuit model fitting based on the DRT result were also employed. The C values of peaks in the DRT diagram can be estimated based on the time constants ( $\tau$ ) reading from the DRT diagram and resistance (R) according to the formula:

$$C = \tau / R \tag{3}$$

Moreover, they can also be calculated based on the equivalent circuit modeling result by the following formula:

$$C = R^{(1-n)/n} Q^{1/n} (4)$$

Where *Q* and *n* are constants obtained from the simulated EIS data. In this paper, the C value of peaks were determined by both methods, the results are shown in Table.S1 (Supplementary Data) and Table.S2 (Supplementary Data), respectively. The C value of the peaks calculated by different methods show the similar order of magnitude. Therefore, the C value calculated based on Eq.1 (shown in Table.S1) were used for the subsequent discussion.

Fig.8 (a) shows the DRT diagram of BZY sample tested in wet hydrogen, and there are two peaks (P1, P2) at the frequency range from 1.2×10<sup>4</sup> Hz to 300 Hz with the relaxation time of 1.798×10<sup>-5</sup> s and 1.783×10<sup>-4</sup> s respectively, representing the bulk and grain boundary processes of the electrolyte. Based on the frequency range information of each peak extracted from the DRT result, a proper equivalent circuit (shown in Fig.6(b)) was chosen for the EIS data fitting and the result shows that the capacitance values of P1 and P2 are in the order of 10<sup>-10</sup> and 10<sup>-9</sup> F, further proving that P1 and P2 are related to the bulk and grain boundary processes of the proton-conducting electrolyte, respectively[31]. Moreover, there are also several peaks observed in the DRT diagram, which should be related to the electrode process. The electrode process is more complex, the peak lying in the low frequency region may be related to the gas transportation process in the porous Pt electrode, and the other peaks may represent the gas conversion process in the electrodes, such as the hydrogen adsorption and dissociation and ionization steps [32, 33, 34]. For the composite electrolyte BG73 tested in reducing atmosphere, there is an extra peak (P3) emerged in the DRT diagram, lying

within the frequency range of the second arc in the Nyquist plot. The second arc represents the grain boundary process of the electrolyte, thus this specific peak, P3, should also be related to the ion transportation through the grain boundaries. Based on the DRT result, the equivalent circuit fitting is conducted with an equivalent circuit model shown in Fig.6 (d). The corresponding C values of P1, P2 and P3 are 4.80×10<sup>-1</sup> <sup>10</sup>, 1.99×10<sup>-9</sup> and 9.17×10<sup>-9</sup> F, respectively. For the first peak, its C value close to the bulk process and the other two peaks should be related to the different grain boundary processes according to the reported works [28, 31]. Previously, Wang et.al. measured the EIS of BCY-SDC composite electrolytes in air and then fitted the data by equivalent circuit models, and found that two different grain boundary processes were determined based on the fitting result [25]. In this work, for the BZY-GDC composite measured in reducing atmosphere, P2 should be the BZY/BZY and GDC/GDC grain boundaries, and P3 is related to the hetero-phase grain boundaries (BZY/GDC interface). The DRT diagram of sample BG55 also has three peaks in the high frequency range as shown in Fig. 8 (c), representing the bulk process and two grain boundaries processes according to their corresponding capacitance value. However, for sample BG 37, as shown in Fig. 8 (d), the C value of P3 is estimated to be 1.56×10<sup>-7</sup> F, a typical capacitance value of the electrode process[24]. There is only one peak (P2) associating with the grain boundary process, with a C value of 3.40×10<sup>-9</sup> F, even if there are still two types of grain boundaries existed. Moreover, from the DRT diagrams of BG73 and BG55, a significant decrease in the third peak (P3) comparing to P2 can be observed. Since the area under the peak in the DRT diagram is proportional to the resistance of the corresponding process[35], this result indicates that the resistance of the hetero-phase grain boundary is decreased with the increase in the GDC content. This can be explained based on the different morphology exhibited in Fig.3. For BG73, the average grain size is small, therefore, the probability of the BZY/GDC contact will be higher than sample BG55, which shows a larger average grain size.

The influence of test temperature on the two different grain boundaries are also investigated, and the impedance data of composite electrolyte BG37 tested from 400 °C to 550 °C was further analyzed and compared, with the DRT results shown in Fig.9. At

lower temperature ( $\leq 450$  °C), there are three peaks lying in the range of the frequency from  $10^6$  Hz to 1258 Hz (shown in Fig.9 (a1)) and  $10^6$  Hz to 1000 Hz (shown in Fig.9 (b1)), respectively. And in the corresponding Nyquist plots (Fig.9 (a2) and Fig.9 (b2)), the first two arcs are just distributed in the same range. Normally, the first two arcs in the Nyquist plot can be interpreted as the bulk and the grain boundary processes. Therefore, at the lower temperature, the three peaks lying in the high frequency range as shown in Fig.9 (a1) and Fig.9 (b2) should represent the bulk and two grain boundaries processes. However, with the increase of the test temperature, there is only one single peak remained (Fig.9 (c1) and Fig.9 (d1)) in the frequency range of the first arc exhibited in the Nyquist plots (Fig.9 (c2) and Fig.9 (d2)) from 10<sup>6</sup> Hz to 10<sup>4</sup> Hz. Since the arc representing the bulk process is supposed to disappear at elevated temperature[28], the arc lying in the frequency range from 10<sup>6</sup> Hz to 10<sup>4</sup> Hz in the Nyquist plots should be solely related to the grain boundary process. Therefore, the single peak in the same frequency range (from 10<sup>6</sup> Hz to 10<sup>4</sup> Hz) in both Fig.9 (c1) and Fig. 9 (d1) should represent the grain boundary process. This result reveals that the two different grain boundary processes can only be separated from the impedance data obtained at lower temperature (\$\leq\$ 450 °C) and similar phenomenon has also been observed by Wang et.al. [25].

## 3.4 Electrical conductivity of the composite electrolyte and cell performance

The temperature dependences of total conductivity of different samples are shown in Fig.10 (Fig.10(a) in air and Fig.10(b) in wet hydrogen). The total conductivity is expressed as  $\sigma_t = \sigma_{bulk} + \sigma_{gb}$ , where  $\sigma_{bulk}$  is the bulk conductivity and  $\sigma_{gb}$  is the total conductivity of grain boundary.  $\ln(\sigma)$  is plotted against the 1000/T, showing a linear relationship, which can be described by the Arrhenius equation:

$$\sigma T = A \exp\left(-\frac{E_a}{RT}\right) \tag{5}$$

Where  $\sigma$  is the conductivity (S/cm), T is temperature (K), R is universal gas constant and  $E_a$  is the activation energy (eV). The activation energy and conductivity of the different samples are calculated and summarized in Table.1. It can be observed that the total conductivity of all samples increases as the increase of the test temperature in both

atmospheres. Moreover, the total conductivity is also enhanced as the content of GDC is increased in the composite electrolyte under both dry air and wet H<sub>2</sub>. In air, the increased total conductivity can be attributed to the higher conductivity of GDC as shown in Fig.10 and Table.1. In reducing atmosphere, the activation energy is lower due to the proton conductivity introduced by wet hydrogen[36]. Moreover, in reducing atmosphere, the activation energy value increases with the increase in the GDC content, due to the fact that GDC becomes a mixed ion and electron conductor in reducing atmosphere (or low oxygen atmosphere) [37], while the activation energy of oxygen ion conductivity is much higher than the proton conductivity of BZY[38]. The total conductivity of the composite samples increases with the increase in GDC content and sample 37BG shows the highest total conductivity up to 0.026 S/cm in wet H<sub>2</sub> at 700 °C, which is smaller than the total conductivity of GDC (0.0558 S/cm) in reducing atmosphere as shown in Table.1. The high conductivity may result from the enhanced conductivity of GDC in reducing atmosphere by the following equation[39].

$$H_{2(g)} + O_0^x \to V_o^{\square} + 2e' + H_2 O_{(g)}$$
 (6)

The total conductivity of GDC is improved due to the removal of oxygen and generation of polaronic electrons[39]. At the same time, the vapor produced during the reduction process may enhance the local concentration of water content, enhancing the proton conductivity of BZY. Fig.10(c) and Fig.10(d) show the bulk and grain boundary conductivity of different samples tested at lower temperature (from 350°C to 500°C) in reducing atmosphere. The grain boundary conductivity is significantly enhanced with the increase in GDC content. However, the corresponding activation energy is decreased, as shown in Table.1, probably attributed to the presence of the hetero-phase boundary. The different crystal structure of GDC (cubic fluorite) and BZY (perovskite) may cause lattice disorder at the interface, leading to a larger activation energy value. Alternatively, it may be resulted from the higher electronic conductivity and oxygen ion activation energy of GDC through the grain boundary in reducing atmosphere.

Due to the highest conductivity of the BG37 among these composite electrolytes, single cell with BG37 electrolyte was fabricated and tested. The cross-sectional SEM

image of the tested cell is exhibited in Fig.11, dense electrolyte with a thickness of 20-30µm can be observed. Fig. 12(a) shows the electrochemical performance of the single cell tested from 600 to 700 °C. The measured open circuit voltages (OCV) of the cell are 0.94, 0.91 and 0.89V at 600, 650, and 700 °C, respectively, and the corresponding peak power densities of the cell are 442 mW/cm² at 700 °C, 300 mW/cm² at 650 °C and 179 mW/cm² at 600 °C, respectively. It can be concluded that the OCV of cell based on composite electrolyte is improved comparing to the cells with the pure GDC electrolyte [40]. Fig. 12(b) shows the EIS spectra of the different cells, the intercepts of the spectra with real axis at high frequencies and low frequencies represent the ohmic resistance and the total resistance of the cell. With the increasing of the operation temperature, both the ohmic resistance and total resistance are decreased. According to the cell performance shown in Fig. 12(a), which is comparable with the reported cells based on the composite electrolytes[23], [25], the BG37 composite electrolyte exhibits great potential to replace the conventional cerium-based electrolyte.

### 4.Conclusion

BZY and GDC ceramic powders were synthesized by a sol-gel method and BZY-GDC composite electrolytes were fabricated by mixing BZY and GDC powders with different weight ratio. The XRD pattern of composite electrolyte shows that BZY and GDC have good chemical compatibility even after sintered at 1550°C for 24 hours. Morphology of the samples was observed using SEM and the average grain size was estimated based on the surface SEM images of the samples. BG73 shows the smallest grain size due to the different grain growth rates of the two ceramics during the sintering process. The electrical conductivity of the samples was determined by measuring the EIS in different atmospheres, the EIS data obtained in humidified hydrogen was analyzed by the distribution of relaxation times (DRT) method. DRT analysis reveals two different grain boundary processes for BG37 and BG55 at lower temperature (\$\leq\$450 °C), which are related to the BZY/BZY and GDC/GDC grain boundaries as well as the BZY/GDC grain boundary. With the increase in GDC content, the BZY-GDC composite sample possesses higher total conductivity and corresponding increase in activation energy in wet H<sub>2</sub>. BG37 shows a total conductivity of 0.026 S/cm in wet H<sub>2</sub>

at 700 °C. Single cell based on BG37 electrolyte shows a good maximum power density of  $0.442~{\rm Wcm^{-2}}$  at 700 °C with considerably high OCV of  $0.89{\rm V}$ .

## Acknowledgments

This work was supported by the Nature Science Basic Research Plan in Shaanxi Province of China (2020JQ-296) and the U.S. National Science Foundation (DMR-1832809).

### References

- [1] E.P. Murray, T. Tsai, S.A. Barnett, A direct-methane fuel cell with a ceria-based anode, Nature, 400 (1999) 649-651.10.1038/23220
- [2] J. Maček, B. Novosel, M. Marinšek, Ni–YSZ SOFC anodes—Minimization of carbon deposition, Journal of the European Ceramic Society, 27 (2007) 487-491.https://doi.org/10.1016/j.jeurceramsoc.2006.04.107
- [3] B.J.M. Sarruf, J.-E. Hong, R. Steinberger-Wilckens, P.E.V. de Miranda, Influence of novel anode design on the performance and coke resistance towards methane directly-fed solid oxide fuel cells, Ceramics International, 46 (2020) 5368-5379.https://doi.org/10.1016/j.ceramint.2019.10.292
- [4] S. de Souza, S.J. Visco, L.C. De Jonghe, Reduced Temperature Solid Oxide Fuel Cell Based on YSZ Thin Film Electrolyte, Journal of The Electrochemical Society, 144 (1997) L35-L37.https://doi.org/10.1149/1.1837484
- [5] Y. Ling, T. Li, Y. Yang, Y. Tian, X. Wang, K. Chen, D. Dong, Y. Chen, K. Amezawa, Oxygen vacancies-rich iron-based perovskite-like electrodes for symmetrical solid oxide fuel cells, Ceramics International, 47 (2021) 12916-12925.https://doi.org/10.1016/j.ceramint.2021.01.154
- [6] M. Mogensen, N.M. Sammes, G.A. Tompsett, Physical, chemical and electrochemical properties of pure and doped ceria, Solid State Ionics, 129 (2000) 63-94.https://doi.org/10.1016/S0167-2738(99)00318-5
- [7] M. Liu, D. Ding, Y. Bai, T. He, M. Liu, An Efficient SOFC Based on Samaria-Doped Ceria (SDC) Electrolyte, Journal of The Electrochemical Society, 159 (2012) B661-B665.https://doi.org/10.1149/2.032206jes
- [8] H. Dai, H. Kou, Z. Tao, K. Liu, M. Xue, Q. Zhang, L. Bi, Optimization of sintering temperature for SOFCs by a co-firing method, Ceramics International, 46 (2020) 6987-6990.https://doi.org/10.1016/j.ceramint.2019.11.134
- [9] S.-K. Kim, Y.-H. Kim, U. Paik, J.-G. Park, Influence of Crystalline Structure of Ceria on the Remaining Particles in the STI CMP, Journal of The Electrochemical Society, 154 (2007) H642.https://doi.org/10.1149/1.2735923
- [10] W. Suksamai, I.S. Metcalfe, Measurement of proton and oxide ion fluxes in a working Y-doped BaCeO3 SOFC, Solid State Ionics, 178 (2007) 627-634.https://doi.org/10.1016/j.ssi.2007.02.003
- [11] A.K. Azad, C. Savaniu, S. Tao, S. Duval, P. Holtappels, R.M. Ibberson, J.T.S. Irvine, Structural origins of the differing grain conductivity values in BaZr0.9Y0.1O2.95 and indication of novel approach to counter defect association, Journal of Materials Chemistry, 18 (2008) 3414-3418.https://doi.org/10.1039/B806190D
- [12] K.-D. Kreuer, Proton Conductivity: Materials and Applications, Chemistry of Materials, 8 (1996) 610-641.https://doi.org/10.1021/cm950192a
- [13] K. Katahira, Y. Kohchi, T. Shimura, H. Iwahara, Protonic conduction in Zr-substituted BaCeO3, Solid State Ionics, 138 (2000) 91-98.https://doi.org/10.1016/S0167-2738(00)00777-3
- [14] S. Wachowski, Z. Li, J.M. Polfus, T. Norby, Performance and stability in H2S of SrFe0.75Mo0.25O3-δ as electrode in proton ceramic fuel cells, Journal of the European Ceramic Society, 38 (2018) 163-171.https://doi.org/10.1016/j.jeurceramsoc.2017.08.020
- [15] S. Le, J. Zhang, X. Zhu, J. Zhai, K. Sun, Sintering and electrochemical performance of Y2O3-doped barium zirconate with Bi2O3 as sintering aids, Journal of Power Sources, 232 (2013) 219-223.https://doi.org/10.1016/j.jpowsour.2013.01.065
- [16] S. Tao, J.T.S. Irvine, Conductivity studies of dense yttrium-doped BaZrO3 sintered at 1325°C, Journal

- of Solid State Chemistry, 180 (2007) 3493-3503.https://doi.org/10.1016/j.jssc.2007.09.027
- [17] H.S. Soares, X. Zhang, I. Antunes, J.R. Frade, G.C. Mather, D.P. Fagg, Effect of phosphorus additions on the sintering and transport properties of proton conducting BaZr0.85Y0.15O3–δ, Journal of Solid State Chemistry, 191 (2012) 27-32.https://doi.org/10.1016/j.jssc.2012.02.053
- [18] L. Ge, J. Jiao, Z. zhu, Q. Zhang, Y. Zheng, H. Chen, L. Guo, A facile method to fabricate proton-conducting BaZr0·85Y0·15O3- $\delta$  electrolyte with a large grain size and high conductivity, Ceramics International, 45 (2019) 24946-24952.https://doi.org/10.1016/j.ceramint.2019.08.202
- [19] D. Gao, R. Guo, Structural and electrochemical properties of yttrium-doped barium zirconate by addition of CuO, Journal of Alloys and Compounds, 493 (2010) 288-293.https://doi.org/10.1016/j.jallcom.2009.12.082
- [20] N. Zuo, M. Zhang, Z. Mao, Z. Gao, F. Xie, Fabrication and characterization of composite electrolyte for intermediate-temperature SOFC, Journal of the European Ceramic Society, 31 (2011) 3103-3107.https://doi.org/10.1016/j.jeurceramsoc.2011.04.030
- [21] H. Bao, R. Chen, X. Wang, Y. Yang, T. Lin, X. Wang, X. Ou, Y. Tian, Y. Ling, Characterization of one-step co-fired BaZr0.8Y0.2O3-δ-La2Ce2O7 composite electrolyte for low-temperature solid oxide fuel cells, Journal of the European Ceramic Society, 41 (2021) 5531-5540.https://doi.org/10.1016/j.jeurceramsoc.2021.04.025
- [22] X.Y. Luo, B. Meng, M.Y. Zhao, H. Xie, L.F. Bian, X. Yang, Preparation and electrical conductivity of BaZr0.8Y0.2O3- $\delta$ /(ZrO2)0.92(Y2O3)0.08 proton/oxygen ion conducting composite ceramic, Ionics, 25 (2019) 1157-1165. https://doi.org/10.1007/s11581-018-2780-3
- [23] K.-Y. Park, T.-H. Lee, S. Jo, J. Yang, S.-J. Song, H.-T. Lim, J.H. Kim, J.-Y. Park, Electrical and physical properties of composite BaZr0.85Y0.15O3–d-Nd0.1Ce0.9O2–δ electrolytes for intermediate temperature-solid oxide fuel cells, Journal of Power Sources, 336 (2016) 437-446.https://doi.org/10.1016/j.jpowsour.2016.11.005
- [24] S. Yu, Z. Wang, L. Yang, J. Liu, R. Guan, Y. Xiao, T. He, Enhancing the sinterability and electrical properties of BaZr0.1Ce0.7Y0.2O3-δ proton-conducting ceramic electrolyte, Journal of the American Ceramic Society, 104 (2021) 329-342.https://doi.org/10.1111/jace.17467
- [25] H. Wang, L. Zhang, X. Liu, H. Bi, S. Yu, F. Han, L. Pei, Electrochemical study on Ce0.85Sm0.15O1.925–BaCe0.83Y0.17O3–δ composite electrolyte, Journal of Alloys and Compounds, 632 (2015) 686-694.https://doi.org/10.1016/j.jallcom.2015.01.135
- [26] X. Zhang, P. Li, Y. Guo, X. Yang, T. Yan, X. Guo, F. Li, Preparation of alumina ultrafine powders through acrylamide, starch and glutaric dialdehyde mediated sol–gel method, Ceramics International, 42 (2016) 6587-6594.https://doi.org/10.1016/j.ceramint.2015.12.146
- [27] M. Shirpour, B. Rahmati, W. Sigle, P.A. van Aken, R. Merkle, J. Maier, Dopant Segregation and Space Charge Effects in Proton-Conducting BaZrO3 Perovskites, The Journal of Physical Chemistry C, 116 (2012) 2453-2461.https://doi.org/10.1021/jp208213x
- [28] J.G. Lyagaeva, G.K. Vdovin, D.A. Medvedev, Distinguishing Bulk and Grain Boundary Transport of a Proton-Conducting Electrolyte by Combining Equivalent Circuit Scheme and Distribution of Relaxation Times Analyses, The Journal of Physical Chemistry C, 123 (2019) 21993-21997.https://doi.org/10.1021/acs.jpcc.9b05705
- [29] A.V. Kuzmin, M.S. Plekhanov, A.S. Lesnichyova, Influence of impurities on the bulk and grain-boundary conductivity of CaZrO3-based proton-conducting electrolyte: A distribution of relaxation time study, Electrochimica Acta, 348 (2020) 136327.https://doi.org/10.1016/j.electacta.2020.136327
- [30] T.H. Wan, M. Saccoccio, C. Chen, F. Ciucci, Influence of the Discretization Methods on the

- Distribution of Relaxation Times Deconvolution: Implementing Radial Basis Functions with DRTtools, Electrochimica Acta, 184 (2015) 483-499.https://doi.org/10.1016/j.electacta.2015.09.097
- [31] J.T.S. Irvine, D.C. Sinclair, A.R. West, Electroceramics: Characterization by Impedance Spectroscopy, Advanced Materials, 2 (1990) 132-138.https://doi.org/10.1002/adma.19900020304
- [32] H. Sumi, H. Shimada, Y. Yamaguchi, T. Yamaguchi, Y. Fujishiro, Degradation evaluation by distribution of relaxation times analysis for microtubular solid oxide fuel cells, Electrochimica Acta, 339 (2020) 135913.https://doi.org/10.1016/j.electacta.2020.135913
- [33] P. Caliandro, A. Nakajo, S. Diethelm, J. Van herle, Model-assisted identification of solid oxide cell elementary processes by electrochemical impedance spectroscopy measurements, Journal of Power Sources, 436 (2019) 226838.https://doi.org/10.1016/j.jpowsour.2019.226838
- [34] J. Xia, C. Wang, X. Wang, L. Bi, Y. Zhang, A perspective on DRT applications for the analysis of solid oxide cell electrodes, Electrochimica Acta, 349 (2020) 136328.https://doi.org/10.1016/j.electacta.2020.136328
- [35] A.K. Baral, Y. Tsur, Sintering aid (ZnO) effect on proton transport in BaCe0.35Zr0.5Y0.15O3- $\delta$  and electrode phenomena studied by distribution function of relaxation times, Journal of the American Ceramic Society, 102 (2019) 239-250.https://doi.org/10.1111/jace.15881
- [36] J. Tong, D. Clark, L. Bernau, M. Sanders, R. O'Hayre, Solid-state reactive sintering mechanism for large-grained yttrium-doped barium zirconate proton conducting ceramics, Journal of Materials Chemistry, 20 (2010) 6333-6341.https://doi.org/10.1039/C0JM00381F
- [37] A. Nenning, C. Bischof, J. Fleig, M. Bram, A.K. Opitz, The Relation of Microstructure, Materials Properties and Impedance of SOFC Electrodes: A Case Study of Ni/GDC Anodes, Energies, 13 (2020).https://doi.org/10.3390/en13040987
- [38] K. Huang, M. Feng, J.B. Goodenough, Synthesis and Electrical Properties of Dense Ce0.9Gd0.101.95 Ceramics, Journal of the American Ceramic Society, 81 (1998) 357-362.https://doi.org/10.1111/j.1151-2916.1998.tb02341.x
- [39] H.A. Al-Madfa, M.M. Khader, M.A. Morris, Reduction kinetics of ceria surface by hydrogen, International Journal of Chemical Kinetics, 36 (2004) 293-301.https://doi.org/10.1002/kin.10186
- [40] Y.D. Zhen, A.I.Y. Tok, S.P. Jiang, F.Y.C. Boey, Fabrication and performance of gadolinia-doped ceria-based intermediate-temperature solid oxide fuel cells, Journal of Power Sources, 178 (2008) 69-74.https://doi.org/10.1016/j.jpowsour.2007.11.113

## **Figure Captions:**

**Figure.1** XRD patterns of BaZr<sub>0.8</sub>Y<sub>0.2</sub>O<sub>3- $\delta$ </sub> (a), Gd<sub>0.2</sub>Ce<sub>0.8</sub>O<sub>2- $\delta$ </sub> (b) and SmBaCo<sub>2</sub>O<sub>5+ $\delta$ </sub> (c) powders calcinated at different temperature for 2 hours.

**Figure.2** XRD patterns of BZY/GDC composite electrolyte sintered at 1550°C for 24 hours.

**Figure.3** SEM images of the surface of sample BZY(a), BG73(b), BG55(c) and BG37(d) sintered at 1550°C for 24 hours.

**Figure.4** SEM images of the fracture of sample BZY(a), BG73(b), BG55(c) and BG37(d) sintered at 1550°C for 24 hours.

**Figure.5** SEM image of BG37 surface (a) and corresponding elemental distribution in the same area for Zr(b), Ce(c), Ba(d) and Gd(e) and the combination of SEM and elemental distribution(f).

**Figure.6** Typical Nyquist plots of the composite electrolytes measured in reducing atmosphere at 350°C (a) and equivalent circuit models applied for EIS data fitting from (b) to (d).

**Figure.7** Nyquist plots of sample BG37 tested at  $350^{\circ}$ C(a),  $400^{\circ}$ C (b),  $450^{\circ}$ C (c) and  $500^{\circ}$ C (d) in wet H<sub>2</sub>.

**Figure.8** DRT curves obtained from EIS spectra of BZY(a), BG73(b), BG55(c) and BG37(d) at 350°C in wet H<sub>2</sub>.

**Figure.9** DRT curves obtained from EIS spectra of BG37 at 350°C(a), 400°C(b), 450°C(c) and 500°C(d).

**Figure.10** Arrhenius plots of the total conductivity of samples tested in air (a) and wet  $H_2$  (10% $H_2$  with Ar) (b), the bulk conductivity of samples tested in wet  $H_2$ (c), and the grain boundary conductivity tested in wet  $H_2$ (d).

**Figure.11** The cross-sectional SEM image of the tested cell with a configuration of NiO-GDC| BG37|GDC-SBCO

**Figure.12** I-V curves and corresponding power densities of test cells with BG37 composite electrolyte (a) and impedance spectra (b) measured at 600-700 °C.

**Table.1** Summary of the total conductivity (in air and wet H<sub>2</sub>) of samples and the corresponding total activation energy values, and the activation energy values of bulk (in wet H<sub>2</sub>) and grain boundaries (in wet H<sub>2</sub>).

Figure.1 XRD patterns of  $BaZr_{0.8}Y_{0.2}O_{3-\delta}$  (a),  $Gd_{0.2}Ce_{0.8}O_{2-\delta}$  (b) and  $SmBaCo_2O_{5+\delta}$  (c) powders calcinated at different temperature for 2 hours.

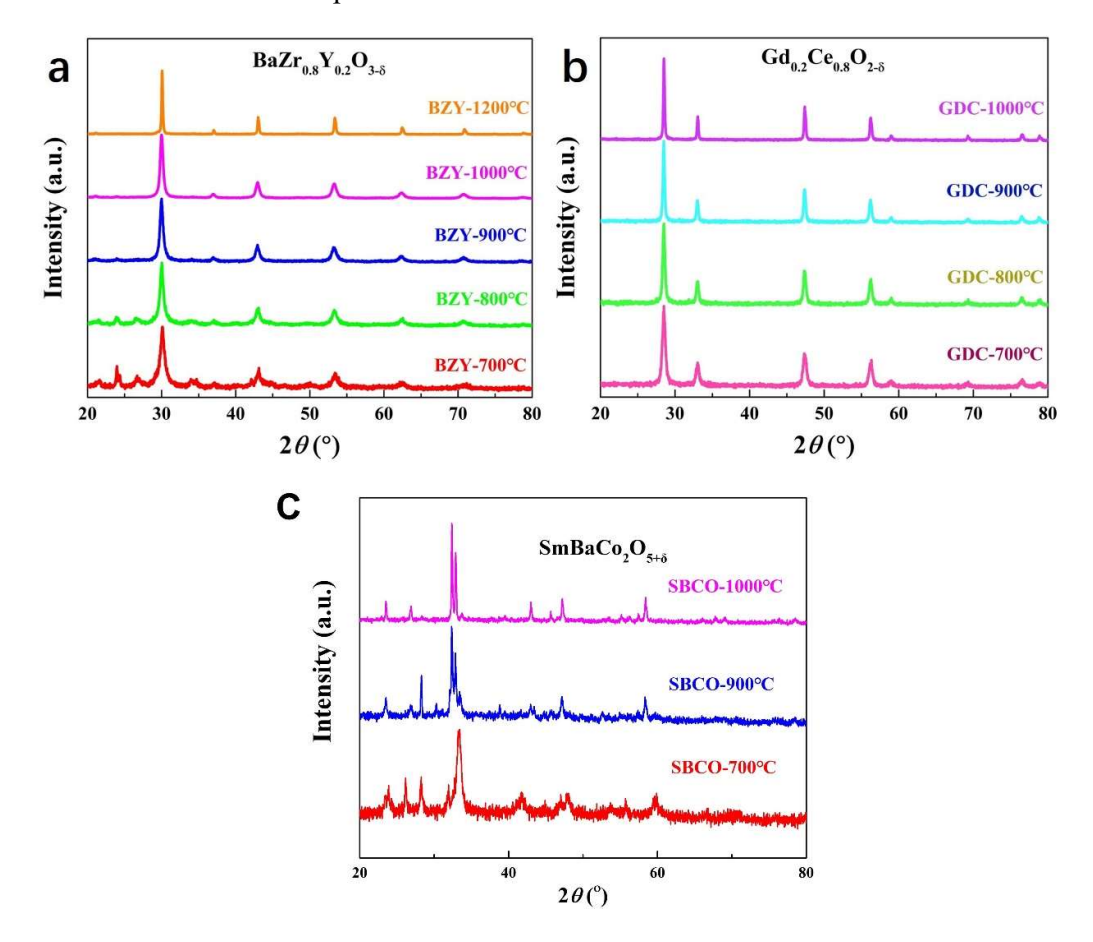


**Figure.2** XRD patterns of BZY/GDC composite electrolyte sintered at 1550°C for 24 hours.

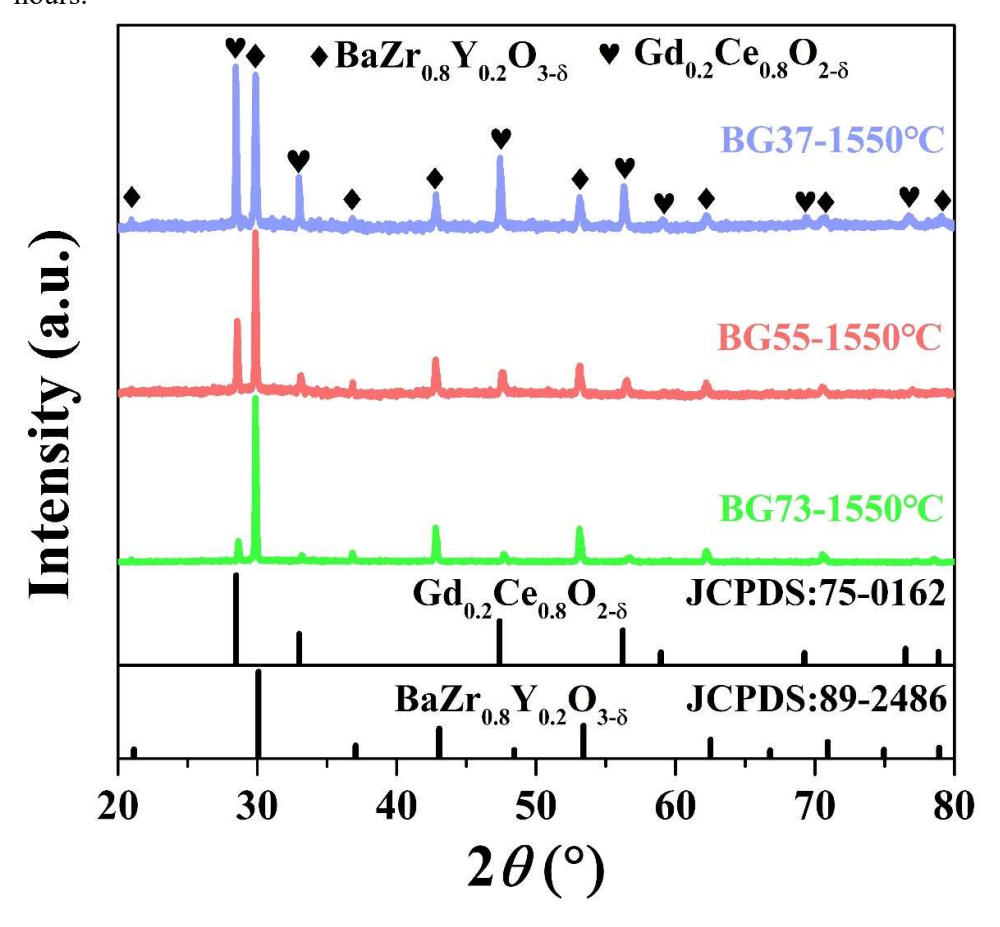


**Figure.3** SEM images of the surface of sample BZY(a), BG73(b), BG55(c) and BG37(d) sintered at 1550°C for 24 hours.

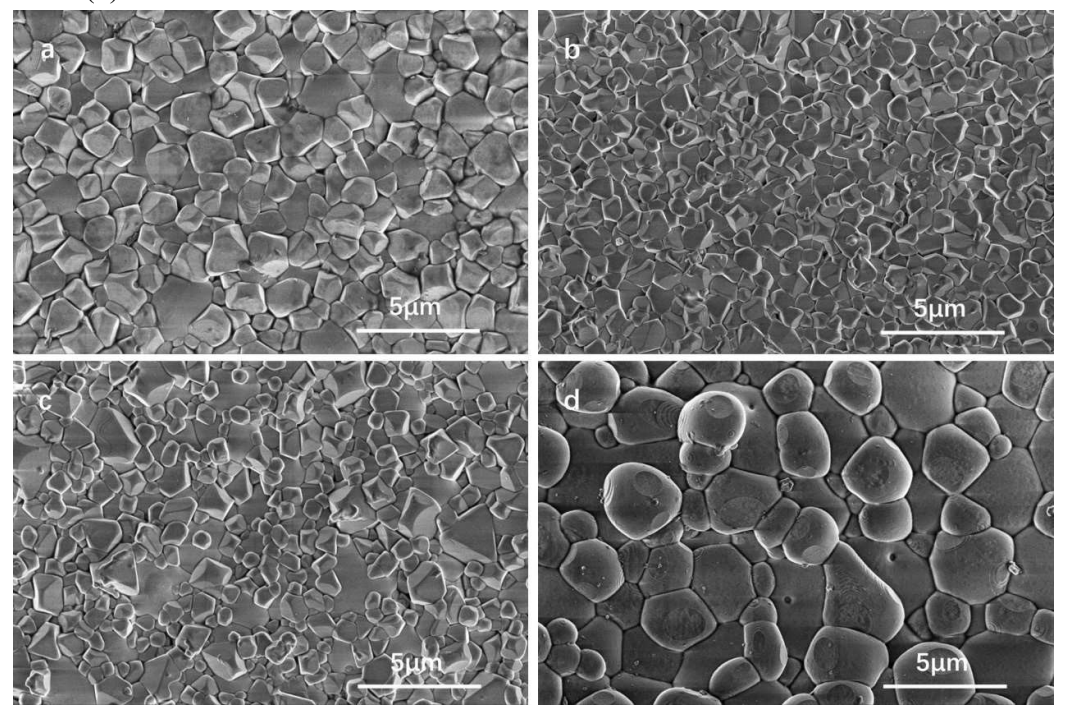


**Figure.4** SEM images of the fracture of sample BZY(a), BG73(b), BG55(c) and BG37(d) sintered at 1550°C for 24 hours.

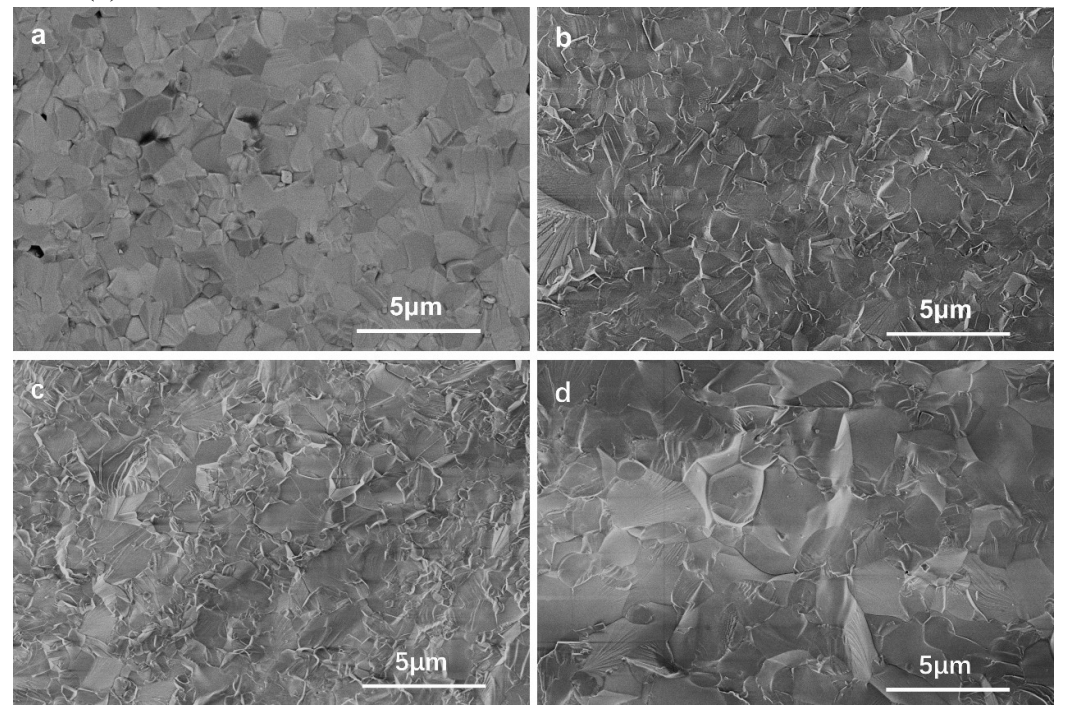


# Figure.5

SEM image of BG37 surface (a) and corresponding elemental distribution in the same area for Zr(b), Ce(c), Ba(d) and Gd(e) and the combination of SEM and elemental distribution(f).

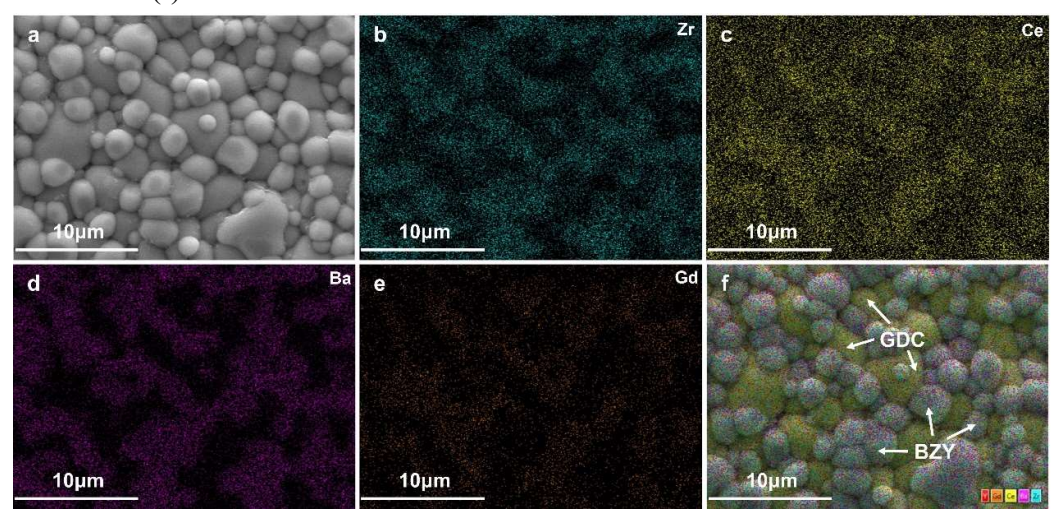
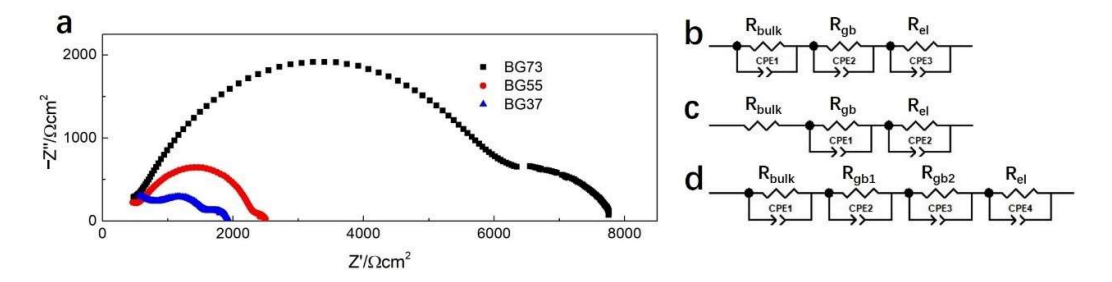
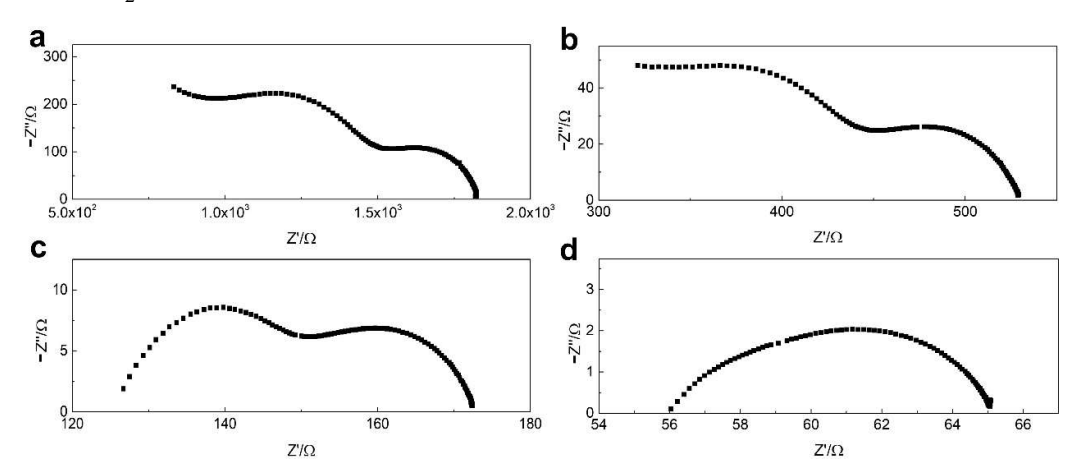


Figure.6

Typical Nyquist plots of the composite electrolytes measured in reducing atmosphere at 350°C (a) and equivalent circuit models applied for EIS data fitting from (b) to (d).



**Figure.7** Nyquist plots of sample BG37 tested at  $350^{\circ}$ C(a),  $400^{\circ}$ C (b),  $450^{\circ}$ C (c) and  $500^{\circ}$ C (d) in wet H<sub>2</sub>.



**Figure.8** DRT curves obtained from EIS spectra of BZY(a), BG73(b), BG55(c) and BG37(d) at 350°C in wet H<sub>2</sub>.

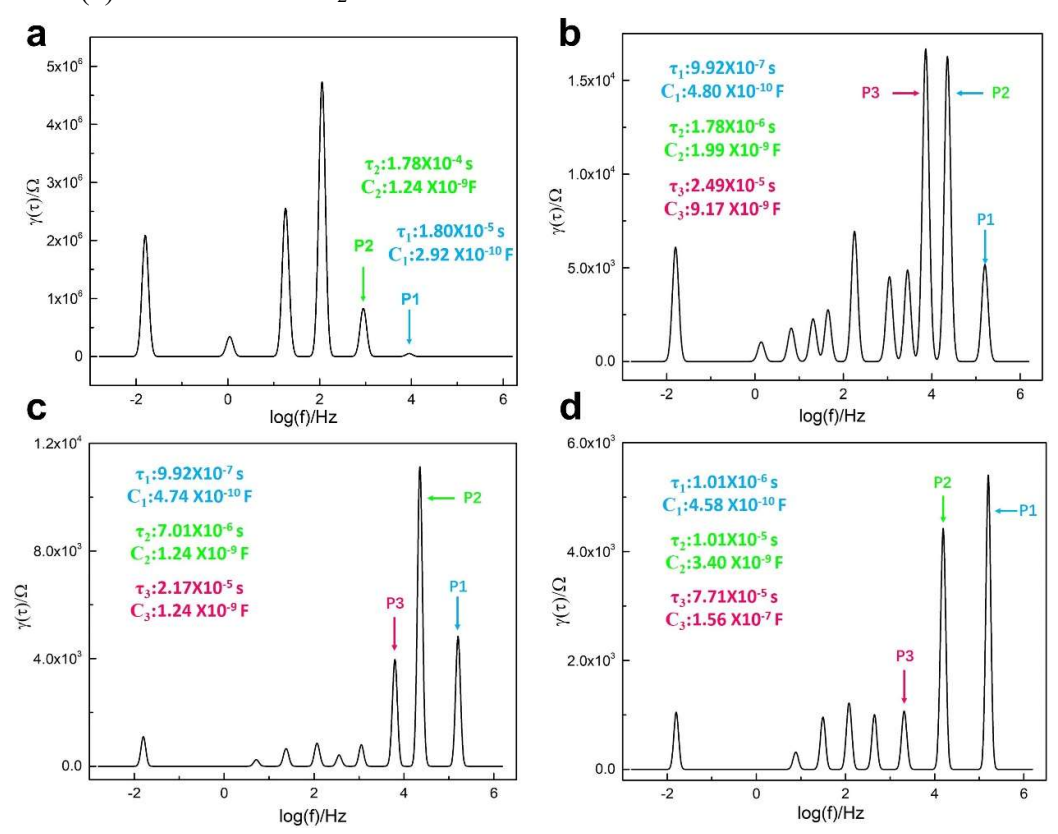


**Figure.9** DRT curves obtained from EIS spectra of BG37 at  $350^{\circ}$ C(a),  $400^{\circ}$ C(b),  $450^{\circ}$ C(c) and  $500^{\circ}$ C(d).

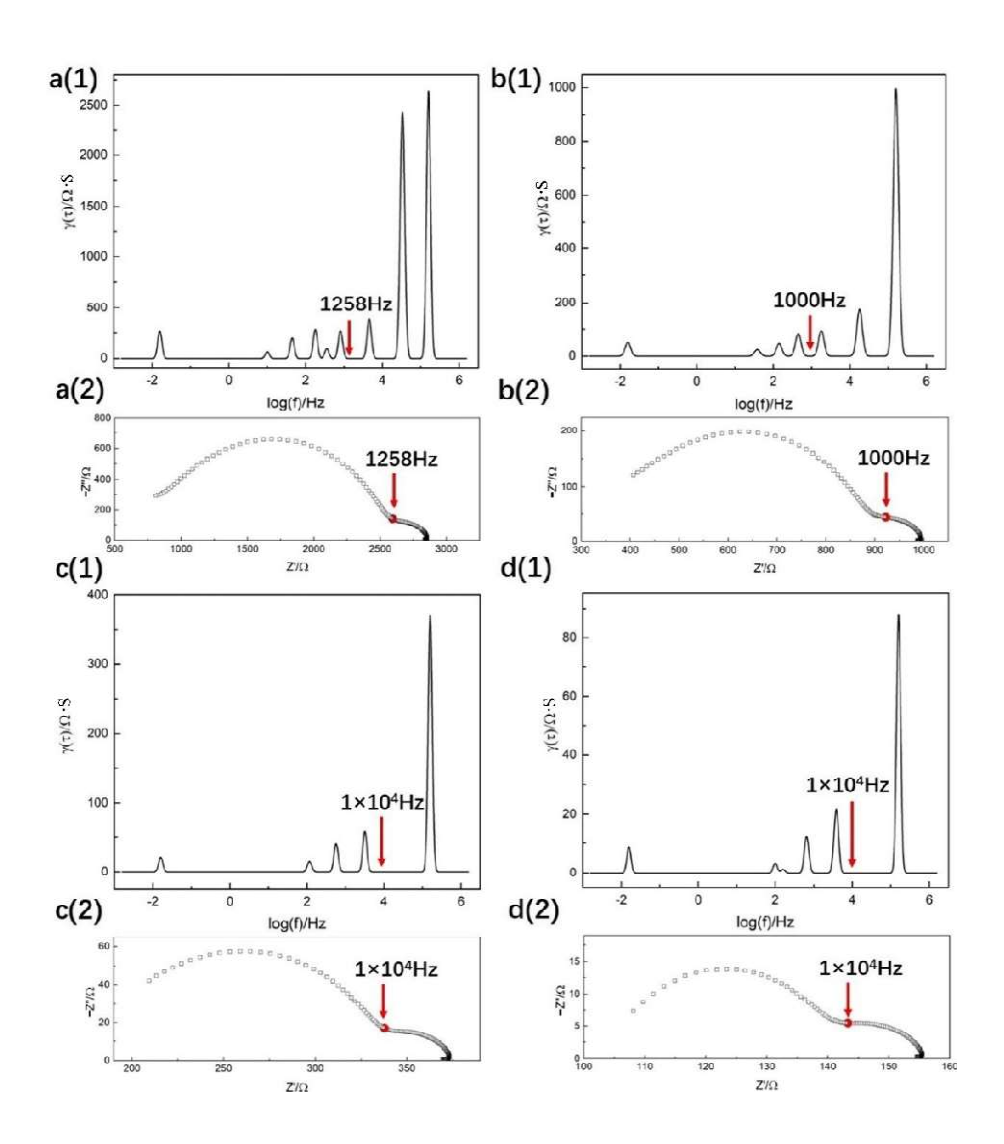
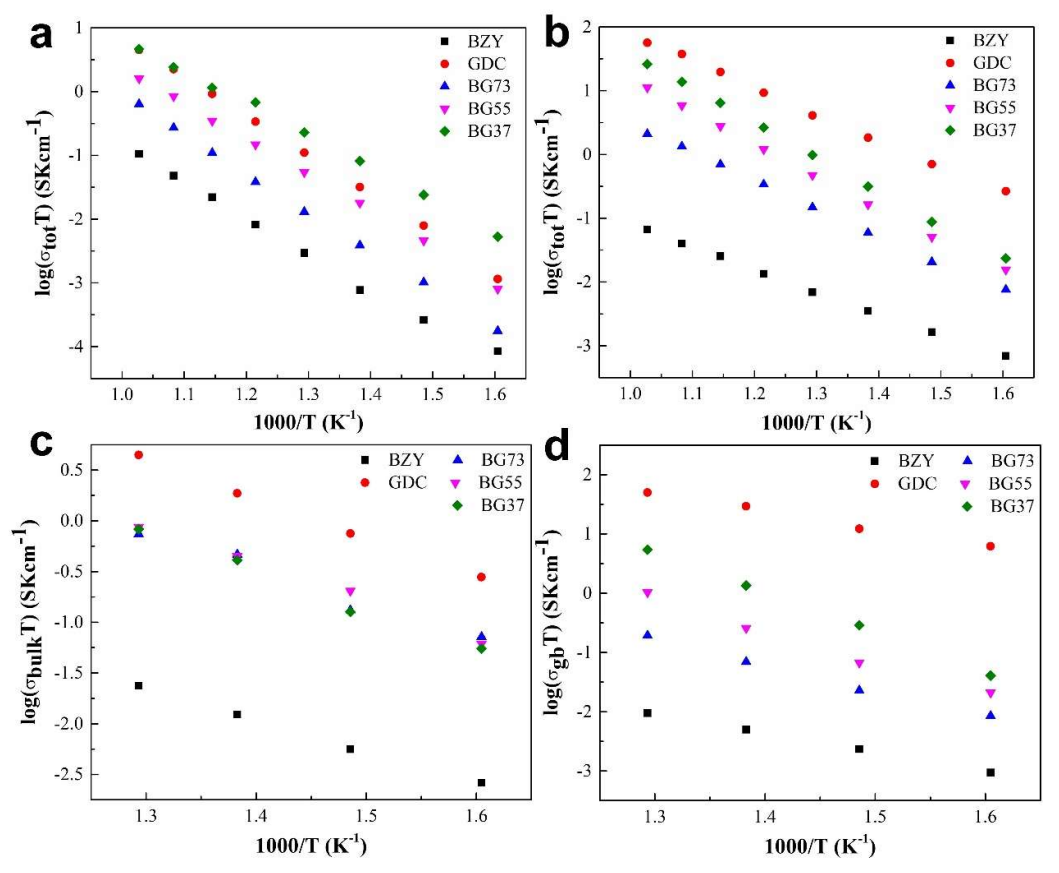
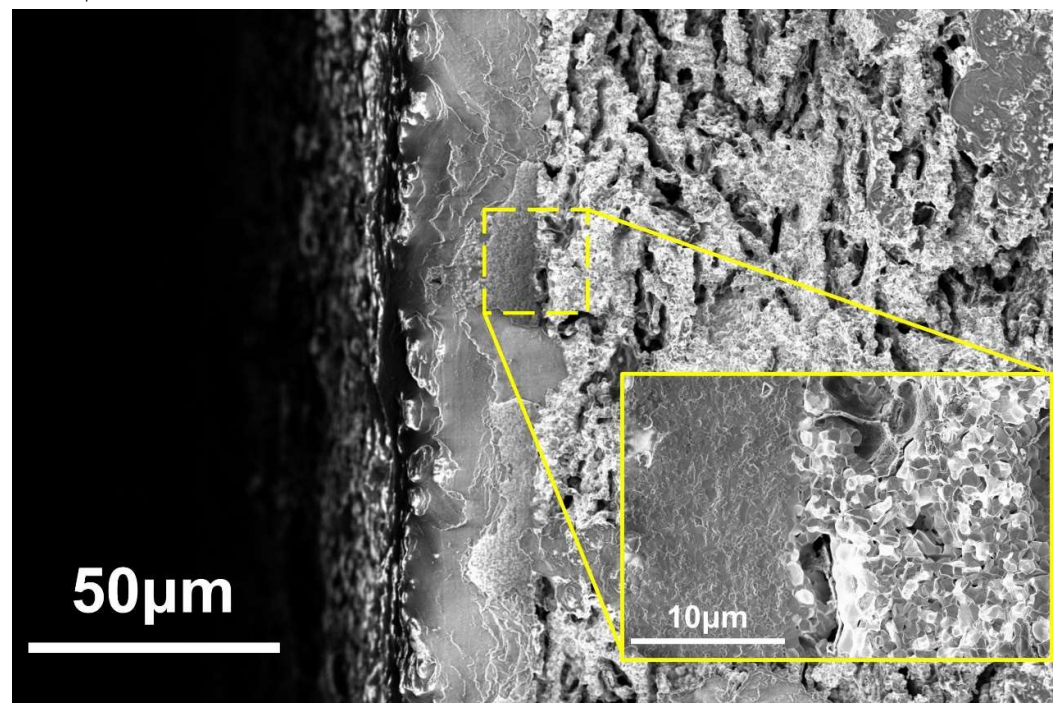


Figure.10 Arrhenius plots of the total conductivity of samples tested in air (a) and wet  $H_2$  (10% $H_2$  with Ar) (b), the bulk conductivity of samples tested in wet  $H_2$ (c), and the grain boundary conductivity tested in wet  $H_2$ (d).



**Figure.11**The cross-sectional SEM image of the tested cell with a configuration of NiO-GDC| BG37|GDC-SBCO



**Figure.12** I-V curves and corresponding power densities of test cells with BG37 composite electrolyte (a) and impedance spectra (b) measured at 600-700 °C.

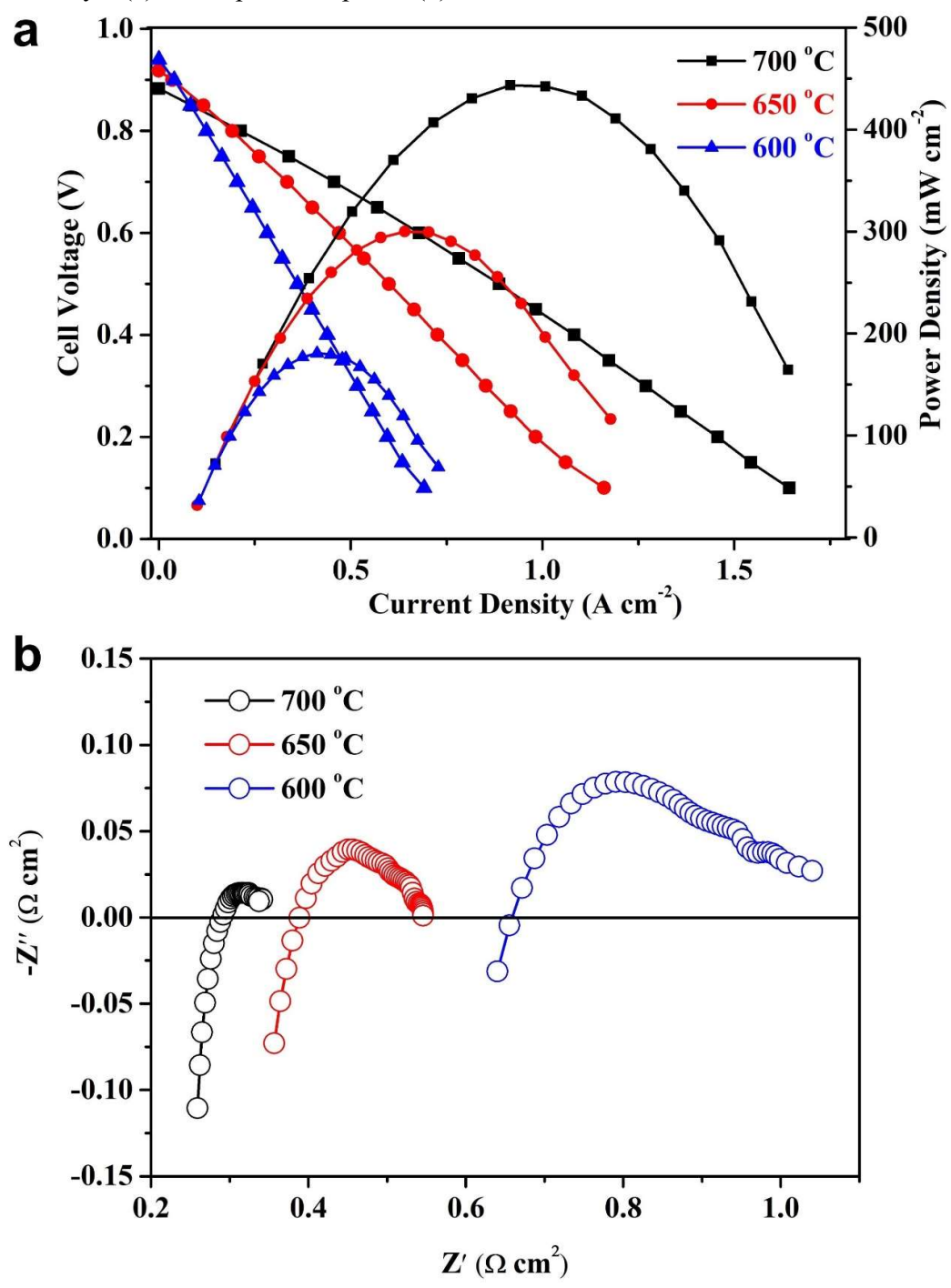


**Table.1** Summary of the total conductivity (in air and wet  $H_2$ ) of samples and the corresponding total activation energy values, and the activation energy values of bulk (in wet  $H_2$ ) and grain boundaries (in wet  $H_2$ ).

Electrolytes	Gaseous	Activation energy/eV			Conductivity(total)/S • cm <sup>-1</sup>
	atmospheres	Total	bulk	Grain	_
				boundary	
BZY	dry air	1.093			1.08×10 <sup>-4</sup>
	wet 5%H <sub>2</sub>	0.687	0.617	0.642	6.86×10 <sup>-5</sup>
GDC	dry air	0.824			4.64×10 <sup>-3</sup>
	wet 5%H <sub>2</sub>	1.235	0.770	0.596	5.58×10 <sup>-2</sup>
BZY <sub>0.7</sub> GDC <sub>0.3</sub>	dry air	1.217			6.54×10 <sup>-4</sup>
	wet 5%H <sub>2</sub>	0.865	0.688	0.872	2.16×10 <sup>-3</sup>
BZY <sub>0.5</sub> GDC <sub>0.5</sub>	dry air	1.131			$1.64 \times 10^{-3}$
	wet 5%H <sub>2</sub>	0.999	0.734	1.084	1.15×10 <sup>-2</sup>
BZY <sub>0.3</sub> GDC <sub>0.7</sub>	dry air	1.011			$4.79 \times 10^{-3}$
	wet 5%H <sub>2</sub>	1.068	0.777	1.357	2.69×10 <sup>-2</sup>